ASCE

A Multiaxial Plasticity Model with Softening for Simulating Inelastic Local Buckling in Steel Beam Columns under Monotonic Loading through Fiber Elements

Diego Isidoro Heredia Rosa[1]; Albano de Castro e Sousa[2]; Dimitrios G. Lignos, M.ASCE[3]; Arka Maity[4]; and Amit Kanvinde, M.ASCE[5]

Abstract: This paper proposes a novel multiaxial plasticity model for 3-dimensional nonlinear static analysis of steel frame buildings with fiber-based beam-column elements. The proposed constitutive formulation is expressed within the framework of rate-independent metal plasticity and captures both the pre- and postpeak response of typical structural steel elements due to yielding and inelastic local buckling under monotonic loading. An initial yield criterion is selected along with newly developed evolution laws. The material response follows J2 plasticity under a tensile stress state. Under compressive loading, the developed constitutive relation incorporates softening to simulate the postpeak response of a member due to inelastic local buckling. The model relies on appropriate yield line mechanisms inferred from buckling analyses of steel plates with characteristic boundary conditions. The proposed constitutive formulation, which is implemented in an open-source frame analysis finite element program, is general and can be used to represent a wide range of softening phenomena. To tackle mesh dependency in the presence of a softening material response, a regularization procedure is developed for 3-dimensional fiber-based elements. Direct comparisons between the predicted and measured nonlinear monotonic responses of physically tested steel beam-columns suggest that the proposed formulation predicts accurately their deduced moment-rotation and the axial shortening-rotation relations. Moreover, the stress distributions across typical cross sections in the postpeak loading regime depict the importance of axial-shear-flexure interaction within a steel beam-column. **DOI: 10.1061/JSENDH.STENG-13136.**

Introduction

Reduced-order models are highly desirable for computing the load-carrying capacity of frame structures. These models are widely used for predicting the performance of new and existing structures (ASCE 2023; CEN 2005b) either with nonlinear static or nonlinear dynamic analysis procedures. In the case of steel structures, which is the primary focus of this thesis, predictive models should capture the strength and stiffness deterioration of steel members. Deterioration mechanisms can be associated with the interaction of different loading modes (e.g., a variable axial force interacting with biaxial flexure, or shear and torsion interacting with axial force and flexure) or with nonlinear geometric instabilities due to local and/or flexural buckling and/or or lateral torsional buckling. While coupling of these nonlinear geometric instabilities may be evident (Kemp 1985; Ozkula et al. 2017b; Elkady and Lignos 2018a), the focus of the present work is on reduced-order models for predicting inelastic local buckling under monotonic loading. It should be noted that failure mechanisms associated with material (e.g., fracture) are out of the scope of this study.

Models of various fidelities have been developed to take into account inelastic local buckling in steel members; namely, (1) point hinge models for flexure; (2) fiber-based beam-column elements; and (3) continuum finite element models. It is also common to use the preceding models in a hybrid fashion (Ribeiro et al. 2015; Hartloper et al. 2022b). Point hinge models for flexure (Ibarra et al. 2005; Lignos and Krawinkler 2011) are computationally efficient, but they exhibit a number of limitations. Particularly, these elements confine inelastic deformation to the ends of the member, thus they are unable to account for inelastic deformations that might occur elsewhere along the length of the element. This is an important consideration when the interaction of axial load and flexure is dominant within a member (MacRae 1989; Ozkula et al. 2017b; Elkady and Lignos 2018a; Suzuki and Lignos 2021). Moreover, point hinge elements for flexure specially tailored to capture local buckling in steel beam column members cannot readily reproduce column axial shortening following the onset of local buckling, which may be an important aspect for a structure from a repairability standpoint (Cravero et al. 2020).

Fiber-based beam-column elements (Taucer et al. 1991; Spacone et al. 1996) can trace the spread of plasticity along with the interaction of axial load and flexure within a member. Moreover, axial shortening in steel columns can be successfully traced when a constitutive material with softening is featured (Suzuki and Lignos 2020). Others have developed 2-dimensional beam-column elements (Saritas and Filippou 2009) that incorporate

[1]Doctoral Assistant, School of Architecture, Civil and Environmental Engineering, École Polytechnique Fédérale de Lausanne, Station 18, Lausanne 1015, Switzerland.

[2]Postdoctoral Researcher, School of Architecture, Civil and Environmental Engineering, École Polytechnique Fédérale de Lausanne, Station 18, Lausanne 1015, Switzerland.

[3]Professor and Chair, School of Architecture, Civil and Environmental Engineering, École Polytechnique Fédérale de Lausanne, Station 18, Lausanne 1015, Switzerland (corresponding author). ORCID: https://orcid.org/0000-0003-0682-4660. Email: dimitrios.lignos@epfl.ch

[4]Doctoral Assistant, Dept. of Civil and Environmental Engineering, Univ. of California, Davis, CA 95616.

[5]Professor, Dept. of Civil and Environmental Engineering, Univ. of California, Davis, CA 95616.

Note. This manuscript was submitted on August 23, 2023; approved on June 13, 2024; published online on October 30, 2024. Discussion period open until March 30, 2025; separate discussions must be submitted for individual papers. This paper is part of the ***Journal of Structural Engineering***, © ASCE, ISSN 0733-9445.

shear-flexure-axial interaction as well as 3-dimensional beam-column elements (Gruttmann et al. 2000; Mazars et al. 2006; Navarro Gregori et al. 2007; Le Corvec 2012; Di Re and Addessi 2018; Maity et al. 2023) to account for shear torsion and warping in addition to flexure and axial load effects.

In structural and continuum mechanics, the use of a constitutive formulation with a distinct behavior under a tensile stress state and another in a compressive one, has been incorporated to capture softening in quasibrittle materials, such as concrete. Particularly, Mander et al. (1988) propose a uniaxial concrete material model that can be used within 2D and 3D beam-column elements, while Lubliner et al. (1989) and Lee and Fenves (1998) propose multiaxial constitutive models for 3D finite element analysis of concrete members. In these cases, the use of damage plasticity in a multiaxial stress state involves a nonassociated plastic flow that results in a non-symmetric material stiffness matrix. Furthermore, in soil plastification the Drucker and Prager (1952) yield criterion is another example of such constitutive formulation.

Moreover, in nonlinear analysis of steel structures, uniaxial material formulations with softening are commonly used in fiber-based beam-column elements (Krishnan 2010; Suzuki and Lignos 2020). It is important to emphasize herein that the softening observed is in an effective sense, i.e., over a finite length of a member owing to inelastic local buckling that occur within this length. Uniaxial material formulations with softening have been developed for simulating the postbuckling behavior of steel reinforcement bars in reinforced concrete members (Gomes and Appleton 1997; Dhakal and Maekawa 2002a, b; Kashani et al. 2015). Varma et al. (2005) and Tort and Hajjar (2010) proposed a material law formulation that can be used within a fiber-based beam-column element to represent the inelastic response of concrete filled steel tubes under monotonic and cyclic loading. Wang et al. (2012) developed a phenomenological uniaxial effective stress-strain constitutive model for wide flange steel beams. Similarly, Bai and Lin (2015) and Bai et al. (2016) proposed a uniaxial constitutive law formulation that exhibits softening in compression under monotonic loading and can be used in fiber-based beam-column elements.

Continuum finite element approaches have been used to simulate the strength and stiffness deterioration mechanisms in steel members subjected to multiaxial loading (Newell and Uang 2008; Fogarty and El-Tawil 2016; Wu et al. 2018; Elkady and Lignos 2018b; Sediek et al. 2020; Hartloper et al. 2022a, b). Due to the associated memory requirements, these models are prohibitively expensive relative to reduced-order finite element modeling approaches (Hartloper 2021) to compute the load-carrying capacity of structures under mechanical loading.

The general consensus from the previous studies is that existing material formulations with softening for fiber-based models are mostly uniaxial. Fiber models even when enhanced with shear and torsional degrees of freedom typically assume a nonevolving shear stress distribution with a constant shear tangent modulus when used with a uniaxial material law along the fiber and an elastic material everywhere else. Therefore, currently, any nonlinear analysis with fiber-based elements that wants to incorporate local buckling in steel members by introducing softening in the material as a proxy, will neglect important member response characteristics corresponding to the interaction of different loading modes (i.e., axial, shear, bending moment, and uniform and non-uniform torsion). In the case of steel beam-columns with wide flange cross sections, the significance of interactive effects has been highlighted experimentally (Ozkula et al. 2017a; Elkady and Lignos 2018a). In capacity-designed steel frame structures, interactive effects become evident after the onset of local buckling.

This paper proposes a multiaxial plasticity formulation to represent inelastic local buckling in steel beam-columns under monotonic loading. Although the focus of the work is on the monotonic response of members with steel wide flange and hollow structural steel (HSS) cross sections, the model formulation is general and can be extended to other softening problems. The model distinguishes between the tensile and compressive behavior in one continuous yield function that evolves independently. Validation studies are presented to demonstrate the suitability of the proposed formulation to predict the postbuckling behavior of steel members with wide flange and HSS cross sections. The examined members are only susceptible to inelastic local buckling, i.e., torsion and warping are not pronounced. Limitations of the proposed formulation are also discussed.

A Multiaxial Constitutive Formulation with Softening for Simulating Inelastic Local Buckling

This section summarizes the primary features of the proposed constitutive formulation with softening. The developed formulation is expressed within the framework of rate-independent metal plasticity (Simo and Hughes 1998). First, a suitable initial yield surface is selected, and then, evolution rules are formulated in order to guide the yield surface evolution conditioned on the respective stress state.

The present formulation distinguishes between tensile (i.e., mean stress, $I_1 > 0$, where $I_1 = \sigma_{ii}$) and compressive stress states ($I_1 < 0$). Local buckling induced softening may only occur under a compressive stress state. Depending on the respective cross-sectional slenderness ratio and the structural steel material, softening may occur prior or after the postyield hardening path. Conversely, tensile loading should only lead to a hardening response after yielding. Referring to Fig. 1, the yield criterion assumed in this work is composed of two different surfaces: (1) the classic von-Mises yield surface in tension [Fig. 1(a)], and (2) an ellipsoid yield surface in compression [Figs. 1(b and c)] that matches the von-Mises yield surface prior to softening. In order to ensure the yield surface continuity on the π-plane (i.e., $I_1 = 0$ in the principal stress space), both the von-Mises and the ellipsoid yield surfaces should have the same radius along that plane. This is shown in Fig. 1(d). The previously mentioned yield surface criterion is formulated mathematically in Eq. (1)

$$\phi = \begin{cases} \phi^{VM}\colon 3J_2 - \sigma_y^2 \leqslant 0 & \text{for } I_1 \geqslant 0 \\ \phi^{ELL}\colon 3J_2 + \chi_{1c} I_1^2 - \sigma_y^2 \leqslant 0 & \text{for } I_1 \leqslant 0 \end{cases} \tag{1}$$

where ϕ^{VM} and ϕ^{ELL} denote the von-Mises and the ellipsoid yield surfaces, respectively, J_2 the second invariant of the deviatoric stress tensor, I_1 the first invariant of the stress tensor, σ_y and σ_c, respectively, denote the yield stress and the stress at capping, χ_{1c} the parameter guiding the ellipsoid yield surface evolution in the softening stage. It should be noted that the function is continuous and differentiable at every point in its surface. The selected yield surface can be seen as an inverted Huber (2004) surface, with the von-Mises cylinder in tension, and an ellipsoid in compression. This ensures the uniqueness of the plastic flow solution at every point on the selected surface, including at the intersection of the tensile and compressive surface on the pi-plane (Kolupaev 2018).

The parameter χ_{1c} controls the evolution of the compressive ellipsoid yield surface radius parallel to the hydrostatic axis (i.e., the axis where $\sigma_1 = \sigma_2 = \sigma_3$). During the elastic and hardening stages in compression, the parameter, $\chi_{1c} = 0$. In those loading stages, the second line of Eq. (1) is the original von-Mises yield surface shown

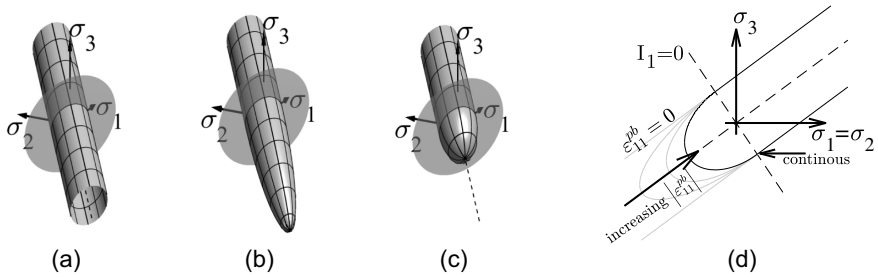

Fig. 1. Yield surface evolution.

in Fig. 1(a). Once the evolution rule for parameter χ_{1c} is selected, a return mapping algorithm is developed in order to find the resulting stress state given an input strain state. The developed return mapping algorithm follows the principles formulated in Simo and Hughes (1998).

Typical 3-dimensional fiber-based beam-column elements (Le Corvec 2012; Di Re and Addessi 2018; Maity et al. 2023), feature three stress and strain components, the axial and the two in-plane shear components. Because the proposed constitutive formulation features a full stress-strain tensor (six independent components due to symmetry), a condensation procedure is required to impose the other three stress components equal to zero as assumed in most 3d-fiber formulations (Le Corvec 2012). In order to reduce the computational cost of fiber-based beam-column elements, an alternative approach to condensation is developed for the case where the stress-strain constitutive law is formulated on the basis of a return-mapping algorithm. This approach is motivated by the enforcement of plane-stress constraints directly in the return mapping algorithm (Simo and Hughes 1998). The stress state of the considered 3d-fibers implies that $\sigma_{23} = \sigma_{22} = \sigma_{33} = 0$. This stress state will be hereafter referred to as multiaxial fiber stress state. The free stress and strain components can be written as the following vectors $\boldsymbol{\sigma} = [\sigma_{11}, \sigma_{12}, \sigma_{13}]^T$ and $\boldsymbol{\varepsilon} = [\varepsilon_{11}, 2\varepsilon_{12}, 2\varepsilon_{13}]^T$. With this definition of the stress and strain vector, Eq. (1) can be rewritten as follows:

$$\phi = \begin{cases} \phi^{VM}\text{: } \dfrac{3}{2}\boldsymbol{\xi}^T\boldsymbol{P}\boldsymbol{\xi} - \sigma_y^2 \leq 0 & \text{for } I_1 \geq 0 \\ \phi^{ELL}\text{: } \dfrac{3}{2}\boldsymbol{\xi}^T\boldsymbol{P}\boldsymbol{\xi} + \chi_{1c}(\boldsymbol{p}^T\boldsymbol{\sigma})^2 - \sigma_y^2 \leq 0 & \text{for } I_1 \leq 0 \end{cases} \tag{2}$$

where $\boldsymbol{\xi} = \boldsymbol{\sigma} - \boldsymbol{\alpha}$ is the relative stress (the backstress component $\boldsymbol{\alpha}$ is defined in the following section). The projection matrix $\boldsymbol{P}$ and projection vector $\boldsymbol{p}$ are given by

$$\boldsymbol{P} = \begin{bmatrix} 2/3 & 0 & 0 \\ 0 & 2 & 0 \\ 0 & 0 & 2 \end{bmatrix} \tag{3}$$

and

$$\boldsymbol{p} = [\,1 \quad 0 \quad 0\,]^T \tag{4}$$

Elastic and Hardening Paths

The present work uses the updated Voce-Chaboche (UVC) plasticity formulation (Hartloper et al. 2021) to model the elastic and hardening loading stages. This hardening law is formulated within the framework of rate independent J2 metal plasticity (Chen and Han 1988; Lubliner 2008). Hereafter, a brief description of the UVC material law is provided. The reader is referred to the original work by Hartloper et al. (2021) for further details.

The kinematic hardening mechanism given in rate form in Eq. (5) has been proposed by Frederick and Armstrong (2007) in order to represent the yield surface translation in the principal stress space

$$\dot{\boldsymbol{\alpha}}_k = \sqrt{\frac{2}{3}} C_k \dot{\varepsilon}^p_{eq} \boldsymbol{n} - \gamma_k \dot{\varepsilon}^p_{eq} \boldsymbol{\alpha}_k \tag{5}$$

where ε^p_{eq} denotes the equivalent plastic strain, $\boldsymbol{n} = (\partial \phi^{VM}/\partial \boldsymbol{\sigma})$ is the normal to yield surface, and C_k and γ_k are material parameters related to the magnitude and rate of the kth backstress component, respectively. The use of multiple backstresses was proposed in Chaboche et al. (1979), where the overall backstress is expressed in Eq. (6)

$$\boldsymbol{\alpha} = \sum_{k=1}^{N_k} \boldsymbol{\alpha}_k \tag{6}$$

Hartloper et al. (2021) proposed the isotropic hardening mechanism in order to represent the yield surface expansion in the principal stress space

$$\sigma_y = \sigma_{y,0} + Q_\infty(1 - \exp[-b\varepsilon^p_{eq}]) - D_\infty(1 - \exp[-a\varepsilon^p_{eq}]) \tag{7}$$

where $\sigma_{y,0}$ is the initial yield stress, Q_∞ and b are material parameters defining the isotropic hardening magnitude and rate, respectively. Similarly, D_∞ and a are material parameters defining the magnitude and rate of the decrease in the initial yield stress. This formulation features the initial yield plateau, which is typically seen in mild structural steels (Lubliner 2008).

For typical mild structural steels, the material parameters $\sigma_{y,0}$, b, Q_∞, D_∞, C_k, and γ_k can be determined from a set of uniaxial monotonic tensile and cyclic coupon tests as discussed in de Castro e Sousa et al. (2020). The experimental data has been made publicly available in Hartloper et al. (2023).

Softening Path

The following two assumptions are made on the yield surface evolution in the postbuckling path: (1) there is no kinematic and isotropic hardening or (2) the evolution of the compressive ellipsoid yield surface is only guided by the evolution of the parameter χ_{1c} [see Eqs. (1) and (2)]. The first assumption implies that the yield surface center and extent in the deviatoric plane remain constant in the softening path, while the second one implies that the ellipsoid yield surface radius parallel to the hydrostatic axis varies.

After the onset of local buckling, the yield surface in compression ($I_1 < 0$) shrinks in order to capture softening. From the second line in Eq. (2), it can be seen that as χ_{1c} increases, the yield surface becomes progressively more oblate, as its radius along the hydrostatic axis reduces. Fig. 1(d) shows the yield surface evolution in the softening path.

The proposed multiaxial formulation with softening can be considered with any evolution rule of χ_{1c}. As such, different ellipsoid yield surface behaviors may be considered, thereby enabling the modeling of different softening responses, if necessary.

It is postulated that the strain vector $\boldsymbol{\varepsilon}$ can be decomposed into a linear sum of strain components according to Eq. (8)

$$\boldsymbol{\varepsilon} = \boldsymbol{\varepsilon}^e + \boldsymbol{\varepsilon}^p + \boldsymbol{\varepsilon}^{pb} \tag{8}$$

where $\boldsymbol{\varepsilon}^e$ is the elastic strain vector, $\boldsymbol{\varepsilon}^p$ is the plastic strain vector and $\boldsymbol{\varepsilon}^{pb}$ is the postbuckling strain vector. The elastic stress-strain relation can then be expressed following Eq. (9)

$$\boldsymbol{\sigma} = \boldsymbol{C}(\boldsymbol{\varepsilon} - \boldsymbol{\varepsilon}^p - \boldsymbol{\varepsilon}^{pb}) \tag{9}$$

where $\boldsymbol{C}$ is the matrix of elastic tangent moduli in the case of the multiaxial fiber stress state.

In the softening path, normality is maintained, thus considering an associative flow rule, the postbuckling strain $\boldsymbol{\varepsilon}^{pb}$ is given by Eq. (10)

$$\dot{\boldsymbol{\varepsilon}}^{pb} = \lambda_{pb} \frac{\partial \phi^{ELL}}{\partial \boldsymbol{\sigma}} \tag{10}$$

where λ_{pb} is the postbuckling consistency parameter, and the term $\partial \phi^{ELL}/\partial \boldsymbol{\sigma}$ represents the normal to the ellipsoid yield surface. By using the ellipsoid yield surface definition, the equivalent postbuckling strain can be defined by Eq. (11)

$$\dot{\varepsilon}^{pb}_{eq} = \lambda_{pb} \sqrt{6 \boldsymbol{\xi}^T_{n+1} \boldsymbol{P} \boldsymbol{\xi}_{n+1} + 8 \chi^2_{1c} (\boldsymbol{p}^T \boldsymbol{\sigma}_{n+1})^2} \tag{11}$$

The constitutive relation for the evolution of χ_{1c} can be formulated independently of the framework for the general softening material response. An application example is shown later for steel plates.

The plasticity constitutive relations and flow rules for the hardening stage are consistent with those of J2 plasticity; the particular details are not presented here for brevity. The reader is referred to Simo and Hughes (1998) and Hartloper et al. (2021) for further details.

Numerical Implementation

In order to implement the developed formulation discussed in the previous section, three different considerations are discussed here: first, the criterion used to distinguish between the different loading stages, second, the procedure used to solve the consistency conditions to obtain the stress state given an input strain vector, and lastly, the derivation of the consistent tangent modulus operator, which ensures a quadratic convergence rate for the solution schemes used in beam-column elements (Hartloper et al. 2021). The subsequent sections summarize important details regarding the previous issues.

Loading Stage Criterion

During loading, a distinction is made between the tensile and compressive loading directions. As previously stated, tensile straining can only result into elastic and hardening stages, which are depicted via the UVC material model. Conversely, during compressive loading, a criterion is needed to consider softening after the elastic and/or hardening stage depending on the corresponding cross-sectional slenderness ratio. This criterion assumes that once the von-Mises stress is equal to the stress, σ_{c0} at capping, then the multiaxial constitutive relation should revert to softening from the original UVC formulation. The stress at capping may be independently calibrated either by using test data or via finite element simulations. An empirical formulation is presented later on (see previous section) for estimating the stress at capping for mild structural steels. Mathematically, the previous criterion can be formulated as follows:

$$\frac{3}{2} \boldsymbol{\sigma}^T \boldsymbol{P} \boldsymbol{\sigma} - \sigma^2_{c0} = 0 \tag{12}$$

where the first term $(3/2)\boldsymbol{\sigma}^T \boldsymbol{P} \boldsymbol{\sigma}$ represents the square of the von-Mises stress. A detailed pseudocode is provided together with the source code that is made publicly available.

Solving the Consistency Conditions

The solution to the consistency condition during the softening stage is addressed by following a methodology analogous to that of classic metal plasticity (Simo and Hughes 1998; Hartloper et al. 2021). Particularly, a return mapping approach is developed for this purpose to determine the stress state resulting from an imposed strain vector. Within such a context, the Kuhn-Tucker complementary conditions are introduced following Eq. (13) in order to define loading in the softening stage or elastic unloading. Specifically

$$\lambda_{pb} \geqslant 0, \qquad \phi^{ELL} \leqslant 0, \qquad \lambda_{pb} \phi^{ELL} = 0 \tag{13}$$

These conditions form the basis of the elastic-predictor-plastic-corrector approach, whereby if the assumed elastic trial state does not respect Eq. (13), then loading in the softening stage is activated, and the return mapping approach determines the postbuckling multiplier λ_{pb}, which constrains the final stress state to the ellipsoid yield surface.

According to Simo and Hughes (1998), the return mapping algorithm consists of an implicit backward Euler time integration procedure, where $t \in [0, t_1, \ldots, T]$ denotes the selected discretized time interval. It is assumed that at time $t = t_n$, the strain state decomposition (i.e., total strain, plastic and postbuckling strain), as well the internal variables governing the yield surface evolution are known.

Eq. (14) shows the algorithmic consistency conditions that should be respected at time increment $t = t_{n+1}$

$$f(\lambda_{pb}) = \frac{3}{2} \boldsymbol{\xi}^T_{n+1} \boldsymbol{P} \boldsymbol{\xi}_{n+1} + \chi_{1c} (\boldsymbol{p}^T \boldsymbol{\sigma}_{n+1})^2 - \sigma^2_y = 0 \tag{14}$$

This equation is solved for time step $t = t_{n+1}$ using the Newton-Raphson Method (Bierlaire 2015) following Eq. (15)

$$\lambda^{(k+1)}_{pb} = \lambda^{(k)}_{pb} - \frac{f(\lambda^{(k)}_{pb})}{Df(\lambda^{(k)}_{pb})} \tag{15}$$

where the linearization of Eq. (14) yields

$$\begin{aligned} Df(\lambda_{pb}) &= \frac{\partial}{\partial \lambda_{pb}} f(\lambda_{pb}) \\ &= [(3\boldsymbol{P}\boldsymbol{\xi}_{n+1}) + 2\chi_{1c} \boldsymbol{p}\boldsymbol{p}^T \boldsymbol{\sigma}_{n+1}] \frac{\partial \boldsymbol{\xi}}{\partial \lambda_{pb}} + (\boldsymbol{p}^T \boldsymbol{\sigma}_{n+1})^2 \frac{\partial \chi_{1c}}{\partial \lambda_{pb}} \end{aligned} \tag{16}$$

with

$$\begin{aligned} \frac{\partial \boldsymbol{\xi}}{\partial \lambda_{pb}} &= \boldsymbol{Q} \boldsymbol{\Gamma}' \boldsymbol{\Lambda}^{-1}_C \boldsymbol{Q}^T [\boldsymbol{\xi}^{trial}_{n+1} - \boldsymbol{C} \lambda_{pb} 2 \chi_{1c} \boldsymbol{p}\boldsymbol{p}' \boldsymbol{\alpha}] \\ &\quad - \boldsymbol{Q} \boldsymbol{\Gamma} \boldsymbol{\Lambda}^{-1}_C \boldsymbol{Q}^T \left[\boldsymbol{C} 2 \chi_{1c} \boldsymbol{p}\boldsymbol{p}' \boldsymbol{\alpha} + \boldsymbol{C} \lambda_{pb} 2 \frac{\partial \chi_{1c}}{\partial \lambda_{pb}} \boldsymbol{p}\boldsymbol{p}' \boldsymbol{\alpha} \right] \end{aligned} \tag{17}$$

where $\boldsymbol{\xi}_{n+1}^{trial}$ denotes the elastic trial stress state, and $\boldsymbol{\Gamma}(\lambda_{pb})$ and its derivative $\boldsymbol{\Gamma}' = (\partial\Gamma/\partial\lambda_{pb})$ are functions of the postbuckling multiplier λ_{pb} given by Eqs. (18) and (19)

$$\boldsymbol{\Gamma}(\lambda_{pb}) = [\boldsymbol{\Lambda}_C^{-1} + \lambda_{pb}(3\boldsymbol{\Lambda}_P + 2\chi_{1c}\boldsymbol{\Lambda}_{pp})]^{-1} \tag{18}$$

$$\boldsymbol{\Gamma}' = \frac{\partial \boldsymbol{\Gamma}}{\partial \lambda_{pb}} = -\boldsymbol{\Gamma}\left[3\boldsymbol{\Lambda}_P + 2\chi_{1c}\boldsymbol{\Lambda}_{pp} + 2\lambda_{pb}\frac{\partial \chi_{1c}}{\partial \lambda_{pb}}\boldsymbol{\Lambda}_{pp}\right]\boldsymbol{\Gamma} \tag{19}$$

The matrices $\boldsymbol{Q}$, $\boldsymbol{\Lambda}_C$, $\boldsymbol{\Lambda}_P$ and $\boldsymbol{\Lambda}_{pp}$ result from the spectral decomposition of the matrix of elastic tangent moduli $\boldsymbol{C} = \boldsymbol{Q}\boldsymbol{\Lambda}_C\boldsymbol{Q}^T$, the projection matrix $\boldsymbol{P} = \boldsymbol{Q}\boldsymbol{\Lambda}_P\boldsymbol{Q}^T$, and projection vector $\boldsymbol{p}\boldsymbol{p}^T = \boldsymbol{Q}\boldsymbol{\Lambda}_{pp}\boldsymbol{Q}^T$.

The procedure described previously is valid for all the evolution laws for the parameter χ_{1c}. Only the derivative $\partial\chi_{1c}/\partial\lambda_{pb}$ should be computed in order to solve the consistency condition provided in Eq. (14). For this purpose, a detailed pseudocode is made available together with the source code of the proposed formulation. Moreover, the reader is referred to Hartloper et al. (2021) for a detailed description of the solution procedure for the consistency conditions during the hardening stage.

Consistent Tangent Modulus

This section provides the tangent modulus operator $d\boldsymbol{\sigma}/d\boldsymbol{\varepsilon}$, which is consistent to the developed return mapping solution scheme for loading in the softening stage. The tangent moduli for loading in the hardening stage can be found in Hartloper et al. (2021).

For clarity, the case where the parameter χ_{1c} is only a function of the postbuckling strain component ε_{11}^{pb} according to Eq. (10) is shown herein. However, this procedure can be generalized for any evolution law of χ_{1c} by linearizing Eq. (14) and by considering the different quantities governing the evolution of χ_{1c}.

The matrix of the consistent elastoplastic tangent modulus operator $\boldsymbol{C}^{ep}$ can be computed using Eq. (20)

$$\boldsymbol{C}^{ep} = \boldsymbol{C}\left(\boldsymbol{I} + \boldsymbol{C}\left(\lambda_{pb}\left(\frac{\partial^2\phi^{ELL}}{\partial\boldsymbol{\sigma}^2} + \boldsymbol{A}\lambda_{pb}\boldsymbol{p}^T\frac{\partial^2\phi^{ELL}}{\partial\boldsymbol{\sigma}^2}\right) - \boldsymbol{D}\left(\frac{\partial\phi^{ELL}}{\partial\boldsymbol{\sigma}} + \lambda_{pb}\boldsymbol{A}\boldsymbol{p}^T\frac{\partial\phi^{ELL}}{\partial\boldsymbol{\sigma}}\right)^T\right)\right)^{-1} \tag{20}$$

where $\boldsymbol{I}$ is the 3×3 identity matrix, and

$$\boldsymbol{A} = \frac{\partial^2\phi^{Comp}}{\partial\boldsymbol{\sigma}\partial\chi_{1c}}\frac{\partial\chi_{1c}}{\partial\varepsilon_{11}^{pb}}B \tag{21}$$

$$\boldsymbol{D} = \left(\frac{\partial\phi^{Comp}}{\partial\boldsymbol{\sigma}} + \frac{\partial\phi^{Comp}}{\partial\chi_{1c}}\frac{\partial\chi_{1c}}{\partial\varepsilon_{11}^{pb}}\lambda_{pb}\boldsymbol{p}^T\frac{\partial^2\phi^{Comp}}{\partial\boldsymbol{\sigma}^2}B\right) \times \left(\frac{\partial\phi^{Comp}}{\partial\chi_{1c}}\frac{\partial\chi_{1c}}{\partial\varepsilon_{11}^{pb}}\boldsymbol{p}^T\frac{\partial\phi^{Comp}}{\partial\boldsymbol{\sigma}}B\right)^{-1} \tag{22}$$

$$B = \left(1 - \frac{\partial\chi_{1c}}{\partial\varepsilon_{11}^{pb}}\lambda_{pb}\boldsymbol{p}^T\frac{\partial^2\phi^{Comp}}{\partial\boldsymbol{\sigma}\partial\chi_{1c}}\right)^{-1} \tag{23}$$

Eq. (20) yields an asymmetric matrix of tangent moduli; therefore, a symmetric approximation is used according to Eq. (24). This approximation by Hopperstad and Remseth (1995) enables the use of optimized solvers and storing strategies for symmetric matrices

$$\boldsymbol{C}_{sym,n+1}^{ep} = \frac{1}{2}((\boldsymbol{C}_{n+1}^{ep})^T + \boldsymbol{C}_{n+1}^{ep}) \tag{24}$$

Application to Inelastic Steel Plate Buckling

The proposed constitutive formulation is tailored to inelastic steel plate buckling under monotonic loading. For this purpose, typical cross-sectional profiles (wide flange and HSS) can be idealized as steel plates with simplified boundary conditions. These idealizations are made to construct suitable yield line mechanisms to analytically represent the local buckling of the previous two steel plate types. It should be noted that these idealizations still exhibit the following approximations: (1) the geometric symmetry of the steel plates, (2) the idealized boundary conditions, and (3) the assumption of constant stresses on the boundaries, which may not hold true when we consider the effects of St Venant torsion on the fibers. The previous assumptions are only considered to infer generic behavioral characteristics that will be subsequently calibrated.

To demonstrate the suitability of the developed constitutive relation with softening to inelastic steel plate buckling, continuum finite element simulations are conducted on steel plates representing the web and flanges of wide flange and HSS cross sections. First, those simulation results are leveraged to develop simplified empirical expressions for estimating the effective stress at capping σ_{c0} [Eq. (12)] based on reference geometric properties of the steel plate of interest. Moreover, the same simulations are used to infer the buckling deformations in the steel plates. The preceding are then used to construct appropriate yield line mechanisms to analytically represent the local buckling mechanisms of steel plates with different boundary conditions. Those yield line mechanisms are then used to formulate the evolution rule of the parameter χ_{1c} guiding the compressive surface evolution during softening once web and flange plate buckling occurs. Finally, the simulation results are used for benchmarking the proposed multiaxial material model formulation.

Finite Element Simulations

Continuum finite element simulations are conducted using ABAQUS (2019). The steel plates to be analyzed reflect cross-sectional slenderness ratios similar to those of highly ductile and moderately ductile members according to AISC (2022). Particularly, web plates with a slenderness ratio $10 \le b/t \le 30$ (where b and t are the width and thickness of the steel plate, respectively) are considered. Similarly, flange plates with a slenderness ratio of $4 \le b/t \le 8$ are considered. In prior work, the plate buckling mechanism has been shown to be solely dependent on the plate slenderness ratio (Möller et al. 1997). Therefore, the reference web and flange plate geometry that is used in the simulations is 360×360 mm and 180×180 mm, respectively.

The simulations follow the modeling guidelines by Elkady and Lignos (2018b). In brief, four-node shell elements with reduced integration (S4R) are used. The adopted mesh size consists of 32 elements along both plate directions. Multiaxial plasticity is considered with the UVC material model (Hartloper et al. 2021). The simulations conducted herein use as a basis A992 Grade 50 structural steel. The material model parameters are identical to those reported in Hartloper et al. (2021). The onset of local buckling is triggered by introducing geometric imperfections proportional to the first buckling mode of the respective steel plate. This mode is determined via a standard buckling eigenvalue analysis prior to the application of the compressive loading. The geometric imperfections are scaled according to the modeling recommendations reported in Hartloper (2021). Residual stresses are neglected in this case. The boundary conditions for the web and flange plates are shown in Fig. 2. From this figure, the four edges

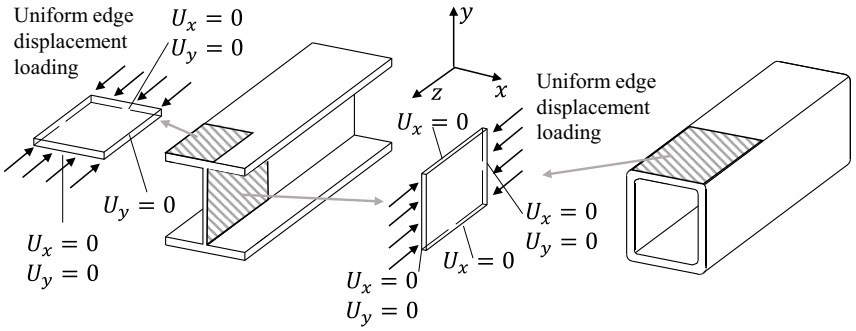

Fig. 2. Boundary conditions of web and flange plates.

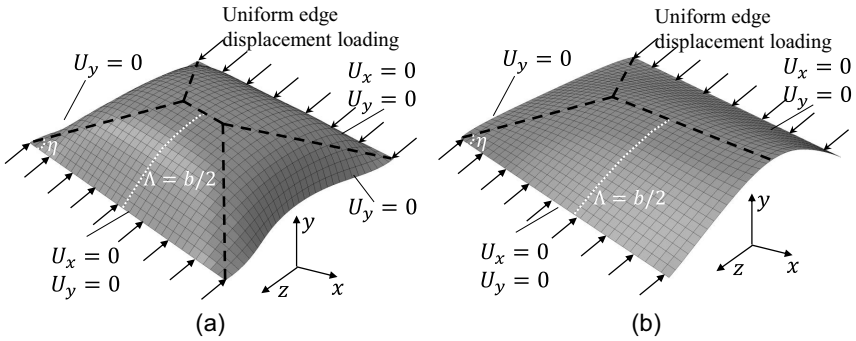

Fig. 3. Buckled shape of plates: (a) web plates; and (b) flange plates.

of a web plate are restrained in the out-of-plane direction, but are free to move in-plane. Conversely, one edge of the flange plate is free in all directions, while the other three edges are restrained in the out-of-plane direction and free in the in-plane direction. For both web and flange plates, two opposing plate edges are loaded in the longitudinal direction using displacement control.

Fig. 3 shows the obtained buckled shapes of the reference web and flange plates. Of interest is an effective stress-strain relationship that can be retrieved from the finite element simulations for uniaxial compression of the corresponding plate as shown in Fig. 4(a) for the web and in Fig. 4(b) for the flange plates. The uniaxial effective stress and strain are defined as follows:

$$\sigma_{eff} = \frac{R}{bt} \quad \text{and} \quad \varepsilon_{eff} = \frac{\delta}{b} \tag{25}$$

where R and δ are the reaction force and the displacement, respectively at the plate edges in the axial direction.

Fig. 5 depicts representative simulations for web and flange plates with different plate slenderness ratios. Qualitatively, the figure suggests that a more compact steel plate exhibits a larger postyield effective plastic strain prior to the onset of local buckling regardless of the respective boundary conditions, as expected. Moreover, relatively slender web plates (e.g., $b/t > 20$) exhibit a steep postbuckling tangent modulus, which is not as evident in flange plates. This is attributed to the differences in the boundary conditions of the two considered steel plate types.

The effective stress-strain relationships shown in Fig. 5 are employed to develop an empirical formulation for predicting the capping stress σ_{c0} as a function of the steel material and the plate geometry. This empirical formulation is established by conventional linear regression analysis (Wasserman 2004). The assumed

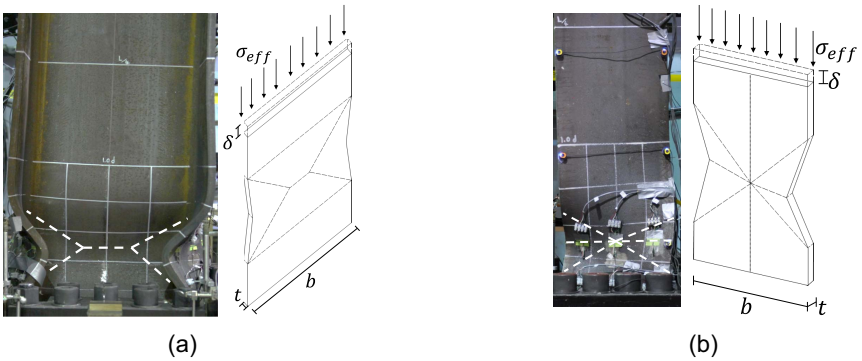

Fig. 4. Plate yield line mechanisms and effective stress-strain definition: (a) web plates; and (b) flange plates. (Images from Elkady and Lignos 2018a.)

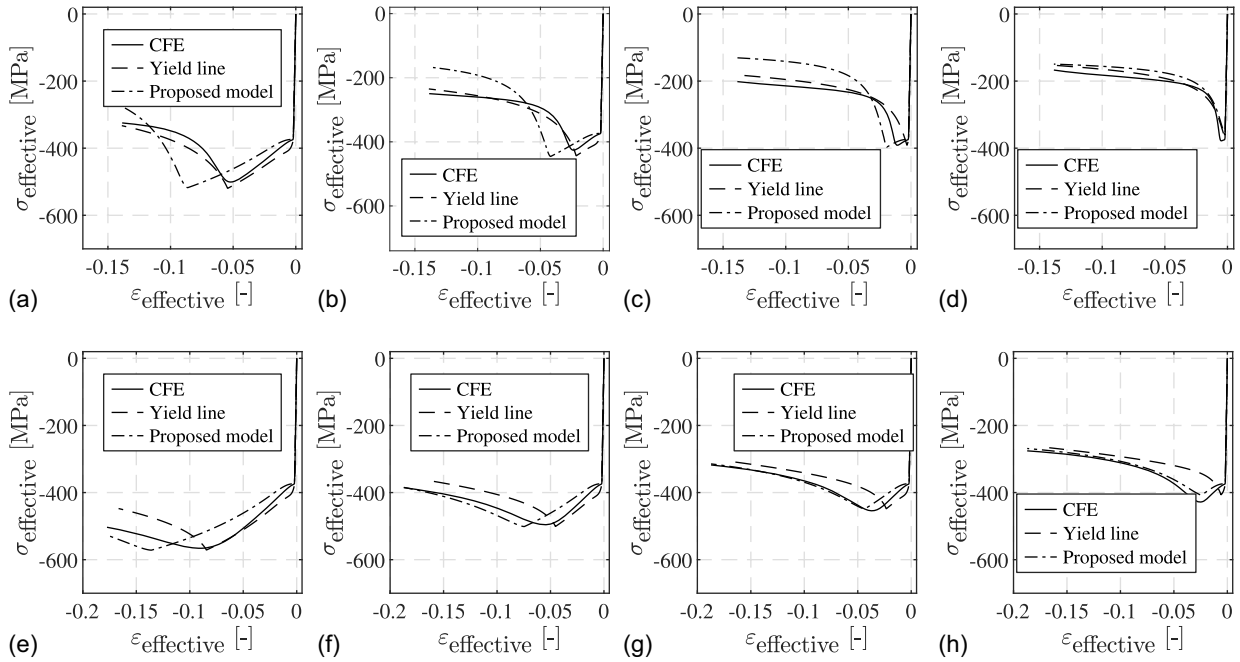

Fig. 5. Comparison of continuum finite element simulations, plate yield line mechanisms and proposed formulation: (a) web plate $b/t = 15$; (b) web plate $b/t = 20$; (c) web plate $b/t = 25$; (d) web plate $b/t = 30$; (e) flange plate $b/t = 5$; (f) flange plate $b/t = 6$; (g) flange plate $b/t = 7$; and (h) flange plate $b/t = 8$.

functional form for σ_{c0} is established according to Eq. (26). In prior work on uniaxial formulations with softening the preceding expression has been found to be effective (Suzuki and Lignos 2020)

$$\frac{\sigma_{c0}}{\sigma_{y0}} = \beta_1 \left(\left(\frac{b}{t} \right) \cdot \sqrt{\frac{\sigma_{y0}}{E}} \right)^{\beta_2} + e \tag{26}$$

where β_1 and β_2 are the empirical regression parameters and e is the error term. Table 1 summarizes the values of β_1 and β_2 obtained for the web and flange plates, as well as the corresponding R^2 values for characteristic structural steels in North America and Europe. From the corresponding R^2 values the functional form represents relatively well the predicted capping stress for different plate geometries. In the presence of interactive buckling (Ozkula et al. 2017b; Elkady and Lignos 2018a) rather than inelastic local buckling, which is addressed herein, the resultant calibration may need to be further tuned. However, this is outside the scope of the present paper.

Table 1. Capping stress regression model parameters

Steel	Regression parameter	Web plates	Flange plates
A992 Gr.50	β_1	1.12	0.54
	β_2	−0.52	−0.70
	R^2	0.96	0.98
A500 Gr.B[a]	β_1	1.13	N/A
	β_2	−0.27	N/A
	R^2	N/A	N/A
S355J2	β_1	1.12	0.62
	β_2	−0.52	−0.60
	R^2	0.99	0.99

[a]Data from Suzuki and Lignos (2020).

Yield Line Mechanism for Analytical Formulation of Plate Buckling

This subsection discusses the yield line mechanisms defined for web and flange steel plates under uniaxial loading in order to formulate the evolution rule of the parameter χ_{1c} of the compressive yield surface in the softening path.

Web plates: The yield line mechanism depicted in Fig. 3(a) is assumed for the web plates. The primary assumptions of this mechanism are that the length $\Lambda = b/2$ does not change during the buckling-induced deformation, and that the angle η between the plate edge and the inclined yield line is equal to 55 °. These assumptions are consistent with prior related work (Möller et al. 1997). In order to formulate the governing equation of this yield line mechanism, the internal work increment dissipated by the mechanism is equated to work increment done by the external load. Recognizing that the total internal work increment comprises the internal work increment dissipated in the inclined yield lines, the one dissipated in the yield line perpendicular to the load, as well as the internal work dissipated by the axial shortening of the two lateral triangles, the internal and external work increments are expressed in Eq. (27)

$$8m_\eta \frac{(1-\varepsilon)}{\sin(2\eta)\sqrt{1-(1-\varepsilon)^2}} + 4m_\perp \frac{b-2c}{b\sqrt{1-(1-\varepsilon)^2}} + \sigma t \sqrt{c^2 + \left(\frac{b}{2}\sqrt{1-(1-\varepsilon)^2} \right)^2} = \sigma t b \tag{27}$$

where m_η and $m_\perp$ are the bending moments per unit length in the inclined yield lines and in the yield line perpendicular to the load, respectively. Eq. (28) depicts the bending moment in a yield line that is inclined with a certain angle θ (Möller et al. 1997)

$$m_\theta(\sigma) = \frac{m_p\left[1-\left(\frac{\sigma}{\sigma_y}\right)^2\right]}{\sqrt{1-\frac{3}{4}[\sin^2(2\theta)+\sin^4(\theta)]\left(\frac{\sigma}{\sigma_y}\right)^2}} \tag{28}$$

where $m_p = (\sigma_y t^2/4)$ is the plastic moment per unit length. Eq. (27) can then be rewritten as follows:

$$\frac{8m_p\left[1-\left(\frac{\sigma}{\sigma_y}\right)^2\right](1-\varepsilon)}{\sqrt{1-\frac{3}{4}[\sin^2(2\eta)+\sin^4(\eta)]\left(\frac{\sigma}{\sigma_y}\right)^2}\sin(2\eta)\sqrt{1-(1-\varepsilon)^2}} + \frac{4m_p\left[1-\left(\frac{\sigma}{\sigma_y}\right)^2\right](b-2c)}{b\sqrt{1-(1-\varepsilon)^2}} + \sigma t\sqrt{c^2+\left(\frac{b}{2}\sqrt{1-(1-\varepsilon)^2}\right)^2} = \sigma t b \tag{29}$$

This nonlinear equation may be solved numerically to find the stress σ given an input strain ε. However, computational efficiency is a key feature to be preserved in the envisioned formulation. Therefore, Eq. (29) is further simplified into an expression that can be solved analytically. Particularly, the following approximation can be made for an angle $\eta = 55°$

$$\frac{3}{4}[\sin^2(2\eta)+\sin^4(\eta)] \approx 1 \tag{30}$$

Simplifying the first term of Eq. (29) and after some basic algebraic manipulations, the following quartic equation is obtained

$$D_w\sigma^4 + E_w\sigma^3 + F_w\sigma^2 + G_w\sigma + H_w = 0 \tag{31}$$

where

$$D_w = -\left(\frac{B_w}{\sigma_y^2}\right)^2 \tag{32}$$

$$E_w = \frac{2B_wC_w}{\sigma_y^2} \tag{33}$$

$$F_w = -\left(\frac{A_w}{\sigma_y}\right)^2 + 2\left(\frac{B_w}{\sigma_y}\right)^2 - C_w^2 \tag{34}$$

$$G_w = -2B_wC_w \tag{35}$$

$$H_w = A_w^2 - B_w^2 \tag{36}$$

with

$$A_w = \frac{8m_p(1-\varepsilon)}{\sin(2\eta)\sqrt{1-(1-\varepsilon)^2}} \tag{37}$$

$$B_w = \frac{4m_p(b-2c)}{b\sqrt{1-(1-\varepsilon)^2}} \tag{38}$$

$$C_w = \left[t\sqrt{c^2+\left(\frac{b}{2}\sqrt{1-(1-\varepsilon)^2}\right)^2} - bt\right] \tag{39}$$

Eq. (31) has a closed form solution. Therefore, the effective stress-strain relation with softening can be analytically derived for a given fiber. Figs. 5(a–d) compare the results from the web plate buckling simulations with those obtained analytically from Eq. (31). The accuracy in all cases is noteworthy.

Eq. (31) can be further modified in order to obtain a similar quartic expression reported in Eq. (40), which can be solved analytically to obtain the σ/σ_y ratio

$$\hat{D}_w\left(\frac{\sigma}{\sigma_y}\right)^4 + \hat{E}_w\left(\frac{\sigma}{\sigma_y}\right)^3 + \hat{F}_w\left(\frac{\sigma}{\sigma_y}\right)^2 + \hat{G}_w\left(\frac{\sigma}{\sigma_y}\right) + \hat{H}_w = 0 \tag{40}$$

where

$$\hat{D}_w = -(\hat{B}_w)^2 \tag{41}$$

$$\hat{E}_w = 2\hat{B}_w\hat{C}_w \tag{42}$$

$$\hat{F}_w = -(\hat{A}_w)^2 + 2(\hat{B}_w)^2 - \hat{C}_w^2 \tag{43}$$

$$\hat{G}_w = -2\hat{B}_w\hat{C}_w \tag{44}$$

$$\hat{H}_w = \hat{A}_w^2 - \hat{B}_w^2 \tag{45}$$

with

$$\hat{A}_w = \frac{A_w}{\sigma_y} = \frac{2t^2(1-\varepsilon)}{\sin(2\eta)\sqrt{1-(1-\varepsilon)^2}} \tag{46}$$

$$\hat{B}_w = \frac{B_w}{\sigma_y} = \frac{t^2(b-2c)}{b\sqrt{1-(1-\varepsilon)^2}} \tag{47}$$

$$\hat{C}_w = C_w = \left[t\sqrt{c^2+\left(\frac{b}{2}\sqrt{1-(1-\varepsilon)^2}\right)^2} - bt\right] \tag{48}$$

The evolution of the σ/σ_y ratio in Eq. (40) as a function of a strain ε may be used to formulate the evolution law for χ_{1c} for the developed multiaxial constitutive response of web plates of various geometries and structural steel materials.

Flange plates: The yield line mechanism of a flange plate is shown in Fig. 3(b). For the flange plate mechanism, it is further assumed that the length Λ does not change as the plate buckling progresses. Moreover, $\eta = 55°$. Expressing the equality between the dissipated internal work increment and the external work increment and by using the approximation from Eq. (30) yields the following quartic equation for the flange plates:

$$D_f\sigma^4 + E_f\sigma^3 + F_f\sigma^2 + G_f\sigma + H_f = 0 \tag{49}$$

where

$$D_f = -\left(\frac{B_f}{\sigma_y^2}\right)^2 \tag{50}$$

$$E_f = \frac{2B_fC_f}{\sigma_y^2} \tag{51}$$

$$F_f = -\left(\frac{A_f}{\sigma_y}\right)^2 + 2\left(\frac{B_f}{\sigma_y}\right)^2 - C_f^2 \tag{52}$$

$$G_f = -2B_fC_f \tag{53}$$

$$H_f = A_f^2 - B_f^2 \tag{54}$$

with

$$A_f = \frac{4m_p(1-\varepsilon)}{\sin(2\eta)\sqrt{1-(1-\varepsilon)^2}} \tag{55}$$

$$B_f = \frac{4m_p(b-c)}{b\sqrt{1-(1-\varepsilon)^2}} \tag{56}$$

$$C_f = \left[\frac{1}{2}t\sqrt{c^2+\left(\frac{b}{2}\sqrt{1-(1-\varepsilon)^2}\right)^2} - bt\right] \tag{57}$$

Figs. 5(e–h) compare the stress-strain relations obtained from the Abaqus plate buckling simulations with those from the yield line mechanism obtained by solving Eq. (49) analytically for the considered flange plates. Similarly to the web plate cases the agreement between the two is noteworthy.

The σ/σ_y ratio can be analytically derived for a given strain ε in a similar fashion with the web plates [see Eq. (58)]. The quartic expression for a flange plate is given in Eq. (58)

$$\hat{D}_f\left(\frac{\sigma}{\sigma_y}\right)^4 + \hat{E}_f\left(\frac{\sigma}{\sigma_y}\right)^3 + \hat{F}_f\left(\frac{\sigma}{\sigma_y}\right)^2 + \hat{G}_f\left(\frac{\sigma}{\sigma_y}\right) + \hat{H}_f = 0 \tag{58}$$

where

$$\hat{D}_f = -(\hat{B}_f)^2 \tag{59}$$

$$\hat{E}_f = 2\hat{B}_f\hat{C}_f \tag{60}$$

$$\hat{F}_f = -(\hat{A}_f)^2 + 2(\hat{B}_f)^2 - \hat{C}_f^2 \tag{61}$$

$$\hat{G}_f = -2\hat{B}_f\hat{C}_f \tag{62}$$

$$\hat{H}_f = \hat{A}_f^2 - \hat{B}_f^2 \tag{63}$$

with

$$\hat{A}_f = \frac{A_f}{\sigma_y} = \frac{t^2(1-\varepsilon)}{\sin(2\eta)\sqrt{1-(1-\varepsilon)^2}} \tag{64}$$

$$\hat{B}_f = \frac{B_f}{\sigma_y} = \frac{t^2(b-c)}{b\sqrt{1-(1-\varepsilon)^2}} \tag{65}$$

$$\hat{C}_f = C_f = \left[\frac{1}{2}t\sqrt{c^2+\left(\frac{b}{2}\sqrt{1-(1-\varepsilon)^2}\right)^2} - bt\right] \tag{66}$$

The evolution of the σ/σ_y ratio as a function of a strain ε is used to formulate the χ_{1c} evolution for the multiaxial constitutive formulation with softening for a flange plate.

Ellipsoid Yield Surface Evolution

In the softening path, the yield surface evolution is guided by the evolution rule for the parameter χ_{1c} [Eqs. (1) and (2)], which in turn is determined from the σ/σ_y ratio for a given strain and plate slenderness ratio according to Eqs. (40) and (58) for web and flange plates, respectively. In the present work, the evolution of this ratio is assumed to be a function of the postbuckling strain component in the axial direction ε_{11}^{pb} defined in Eq. (10). Finally, the evolution of χ_{1c} ratio is determined according to Eq. (67)

$$\chi_{1c} = b_{1c}\left(1 - \frac{\sigma}{\sigma_y}(|\varepsilon_{11}^{pb}|)\right)^2 + c_{1c} \tag{67}$$

where c_{1c} is a constant term used in order to enable buckling prior to yielding, which could very well be the case for noncompact steel plates (i.e., Class 4 according to the European cross section classification (CEN 2005a). Once the capping stress $\sigma_{c0} < \sigma_{y0}$ is attained, the constant c_{1c} is determined such that the compressive ellipsoid yield surface is reached for the specific stress state as determined by Eq. (12). The term b_{1c} is given by the following

$$b_{1c} = \frac{\sigma_{c0}^2}{(\sigma_{c0}^2 - \sigma_{dm}^2)(\alpha_{1c})^2} \tag{68}$$

where α_{1c} is a free parameter, closely related to the stress triaxiality in the plates yield lines. Fig. 6 shows an example of the absolute value of the stress triaxiality in the web and flange plates during the softening stage. From this figure, α_{1c} may be assumed to be equal to 1/3 and 2/3 for the web and flange plates, respectively.

Referring to Eq. (68), σ_{dm} represents the stress at which there is stabilization of the buckling length within a dissipative zone (Krawinkler et al. 1983). A value $\sigma_{dm} = 10$ MPa may be empirically assumed based on prior studies with emphasis at large deformations of structural steel members (Suzuki and Lignos 2020, 2021).

The evolution rule for χ_{1c} as reported in Eq. (67) may be used within the proposed multiaxial constitutive formulation as discussed earlier in the previous section. This can be achieved by computing the required derivatives of χ_{1c} to fully define the return mapping algorithm, as well as the consistent tangent modulus discussed earlier. These derivatives are defined in Eqs. (69) and (70)

$$\frac{\partial \chi_{1c}}{\partial \varepsilon_{11}^{pb}} = 2b_{1c}\left(1 - \frac{\sigma}{\sigma_y}(|\varepsilon_{11}^{pb}|)\right)\frac{\partial}{\partial \varepsilon_{11}^{pb}}\left(\frac{\sigma}{\sigma_y}\right) \tag{69}$$

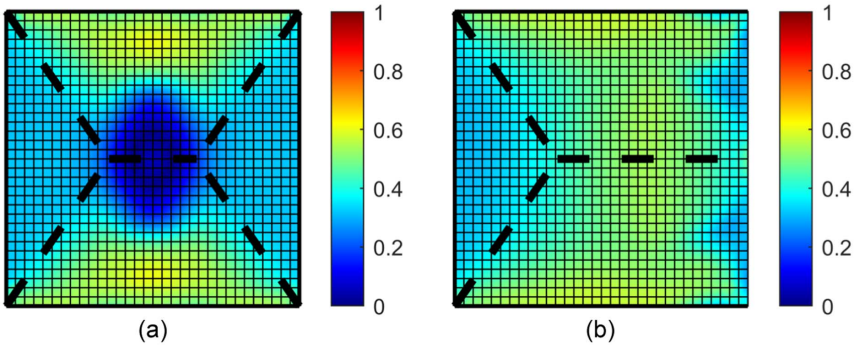

Fig. 6. Stress triaxiality in plate yield lines: (a): web plates; and (b) flange plates.

$$\frac{\partial \chi_{1c}}{\partial \lambda_{pb}} = \frac{\partial \chi_{1c}}{\partial \varepsilon_{11}^{pb}} \boldsymbol{p}^T \frac{\partial \phi^{ELL}}{\partial \boldsymbol{\sigma}} \tag{70}$$

where the partial derivative $(\partial/\partial\varepsilon_{11}^{pb})(\sigma/\sigma_y)$ is obtained from Eqs. (40) or (58) using a complex step derivative approximation (Martins et al. 2003).

The associated pseudo-code of the return mapping algorithm for the softening stage is provided together with the source code in order to replicate the local buckling induced softening behavior of web and flange plates within a cross section. The developed multiaxial constitutive formulation with softening has been implemented in OpenSees version 3.3.0 (McKenna 1997). The developed algorithm and the commands necessary to utilize the developed multiaxial constitutive formulation with softening within OpenSees are provided in Heredia Rosa (2024). The source code in MATLAB is also made available in GitHub (Heredia Rosa et al. 2023 https://github.com/RESSLabTeam/MonotonicPlateBucklingModel).

Fig. 5 contrasts the effective stress-strain relation obtained with the return mapping formulation (termed Proposed model) with those obtained from Abaqus and the yield line mechanism for the web and flange plates. The results for the proposed model are obtained by inputting the following strain vector to the return mapping algorithm discussed earlier

$$\boldsymbol{\varepsilon} = [\,\varepsilon_{11} \quad 2\varepsilon_{12} \quad 2\varepsilon_{13}\,]^T = [\,\varepsilon_{\text{effective}} \quad 0 \quad 0\,]^T \tag{71}$$

The input model parameters to consider combined isotropic/kinematic hardening are taken from Hartloper et al. (2021) for A992 Grade 50. The capping stress σ_{c0} is obtained by using Eq. (26) along with the parameters reported in Table 1. The return mapping algorithm assumes a tolerance tol$= 10^{-6}$ for the convergence criterion.

Referring to Figs. 5(a and b), for very compact web plates ($b/t \leq 20$), there is a difference between the results obtained with the Proposed model and those from the Abaqus plate simulations whereas the predictions based on the assumed yield line mechanism are generally better. One reason for this relates to the empirical nature of equation [Eq. (26)] used to determine the capping stress of web plates with different local slenderness ratios. For instance, from Figs. 5(a and b), the predicted capping stress is noticeably higher than that obtained from the Abaqus simulations. Another reason is the fact that the stress state of compact web plates is considerably different than that of the assumed uniaxial stress state resulting from the assumed uniaxial input vector of Eq. (71). Conversely, for slender web plates [see Figs. 5(c and d)], the proposed formulation agrees fairly well with the Abaqus results as well as the analytically derived formulation with the assumed yield line mechanism. Referring to Figs. 5(e–h) same observations hold true for the flange plates regarding the accuracy of the proposed formulation.

Regularization Procedure to Mitigate Mesh-Dependency in Fiber-Based Elements

It is generally known that in the presence of softening section constitutive relations (i.e., softening material response) such as those presented herein, strain localization and loss objectivity is common in fiber-based beam-column elements (Coleman and Spacone 2001; Sideris and Salehi 2016; Kolwankar et al. 2018). Among different options, one approach to tackle mesh dependence is to formulate a regularization procedure. While the regularization procedure presented herein is general for any 3-dimensional fiber-based beam-column elements, a force-based beam-column element is used to demonstrate the proposed approach. Within such a context, a regularization procedure is proposed, which is motivated by earlier work as summarized in Coleman and Spacone (2001) for reinforced concrete beam-column elements. For brevity, the proposed procedure is illustrated for a web plate with a slenderness ratio of $b/t = 22.3$.

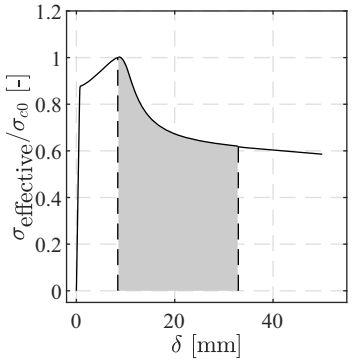

Fig. 7. Normalized axial stress - displacement relation and dissipated energy G of a plate simulated in Abaqus. Dissipated energy is quantified for mesh-dependency regularization.

A reference dissipated energy G should first be determined that corresponds to the softening stage. This energy may be determined either from finite element simulations or physical experiments on steel plates under uniaxial compression. The reference dissipated energy G is defined as the area under the normalized stress-displacement curve shown in Fig. 7. The capping point is used as the starting point, whereas the end point is considered to be that at which postbuckling stress stabilization occurs. Mathematically, this point is defined as the stress at which the tangent modulus becomes constant. Referring to Fig. 7, the value of the ratio $(\sigma/\sigma_{c0})|_{stab}$ corresponding to the postbuckling stabilization point should also be determined. Mathematically, this point is defined as the stress at which the tangent modulus of the corresponding effective stress-strain relation begins to exhibit a constant rate of change. This is achieved when the second derivative of the corresponding effective-strain relation becomes constant, with a value less than 1 MPa.

In order to regularize the developed constitutive formulation with softening, a parameter α_{reg} is used to multiply the strain ε_{11}^{pb} that is inputted into Eq. (40) to compute the evolution of the σ/σ_y ratio. Within a fiber-based beam-column element and for a given quadrature rule, the dissipated energy G shown in Fig. 7 can be expressed in terms of stress and strain using Eq. (72)

$$G = L_{IP} \int \frac{\sigma}{\sigma_{c0}} d\varepsilon \tag{72}$$

where L_{IP} is the length of the integration point for which strain localization is expected.

The integral in Eq. (72) corresponds to the area under the curve defined by the quartic yield line Eq. (40); therefore, it can be expressed as

$$G = L_{IP} \int_0^{\varepsilon_{11}^{pb,*}} \frac{\sigma}{\sigma_y} (\alpha_{reg} \cdot |\varepsilon_{11}^{pb}|) d\varepsilon_{11}^{pb} \tag{73}$$

where $\varepsilon_{11}^{pb,*}$ indicates the value of the postbuckling strain component corresponding to the $(\sigma/\sigma_{c0})|_{stab}$ ratio.

As the dissipated energy G is known, Eq. (73) can be solved for a given L_{IP} in order to determine the regularization parameter α_{reg}.

Validation with Physical Tests on Steel Beam-Columns

In this section, the proposed constitutive formulation is employed within the 3-dimensional Timoshenko force-based beam-column element that is available in OpenSees (McKenna 1997). Specifically, this element follows the element state determination procedure described in Spacone et al. (1996) for a 3-dimensional Euler-Bernoulli beam element and is enhanced by assuming the section state determination discussed in Di Re (2017) in the case of a Timoshenko fiber-based beam-column element with a constant shear strain distribution due to bending. Because the present paper focuses on the multiaxial constitutive formulation with softening, the constant shear strain distribution is deemed acceptable and allows to capture the interaction between the axial and shear forces by accounting for the interaction between longitudinal and shear stresses at the fiber level.

The corotational formulation (Crisfield 1991) is used in order to account for nonlinear geometric effects. This formulation can be used with any 3-dimensional beam-column element as it considers the displacement at the element end node degrees-of-freedom. Furthermore, since the scope of this paper is on the development of the multiaxial softening material law, the effect of this corotational formulation with specific loading modes such as shear, is outside the scope of the present work. The simulation results are compared with those from experimental data on representative steel beam-columns featuring HSS and wide flange profiles under monotonic loading. The comparisons are based on the deduced moment - rotation as well as axial shortening - rotation relationships. For comparison purposes, the results are compared with those derived from continuum finite element simulations in Abaqus.

The experimental data comprise cantilever beam-columns featuring two different cross-sectional profiles; namely, a HSS254x9.5 made of A500 Grade B steel ($D/t = 24.7$, where D and t are the depth and thickness of the HSS, respectively) and a W16x89 made of A992 Grade 50 steel (i.e., web slenderness ratio, $d/t_w = 25.9$; where d and t_W is the web depth and thickness, respectively; and a flange slenderness ratio, $b_f/2t_f = 5.9$; where b_f and t_f is the width and thickness of the flange, respectively). The former is used in specimen H27MC from Suzuki and Lignos (2021), whereas the latter is used in specimen B1 from Cravero et al. (2020). Both specimens where subjected to monotonic lateral load coupled with a constant axial load demand of $P = 0.3P_y$. Steel members featuring wide flange shapes may be susceptible to torsion and warping. In this case, the use of more advanced 3-dimensional beam-column elements (Le Corvec 2012; Maity et al. 2023) would be suitable. However, specimen B1 is laterally braced at $L_b = 1825$ mm from the fixed end [see Fig. 8(a)], resulting into a relatively small, unbraced member length, $L_b/r_y = 37.9$; hence, the test specimen did not experience any torsional demands and softening was only attributed to the formation of cross-sectional local buckling at a distance of about 1.1D from the fixed end. Consequently, the use of the selected 3-dimensional Timoshenko beam element is justifiable in this case. Specimen H27MC is braced at $L_b = 1525$ mm from the bottom end.

Both test specimens are idealized with the force-based beam-column element shown in Fig. 8(b). Five integration points are considered along the element length [see Fig. 8(b)]. The number of integration points along the member length is selected such that their distance is larger than a characteristic length scale. This is taken as the HSS and wide flange local buckling lengths, which, according to Suzuki and Lignos (2021), should be $1.0D$. The

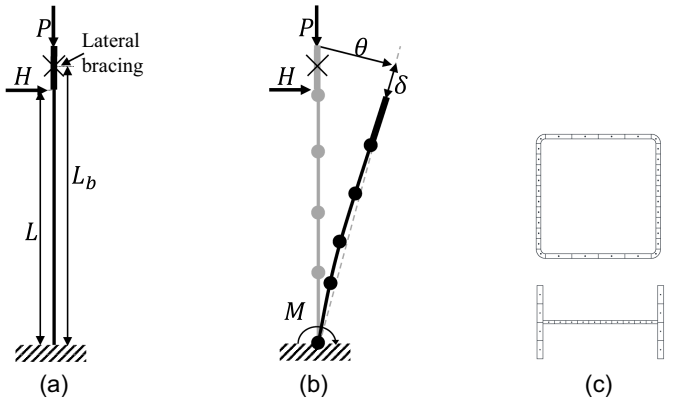

Fig. 8. Model validation with steel column tests: (a) experimental setup; (b) beam-column element; and (c) fiber sections.

Newton-Cotes quadrature rule (Abramowitz and Stegun 1965) is employed.

The HSS and wide flange cross sections are discretized into the fiber sections shown in Fig. 8(c). Each fiber is assigned with the developed constitutive relation with softening. A distinction is made between fibers within a web and a flange plate so that the corresponding relation is assigned as discussed earlier. The regression parameters β_1 and β_2 for estimating the capping stress σ_{c0} using Eq. (26) are taken from Table 1 conditioned on the structural steel type. The capping stress is determined according to Eq. (26). For the HSS profile, the depth is assumed to be equal to $D - 2r$, where r is the corner radius of the HSS. Similarly, a depth equal to $d - 2t_f - 2r$ is used for the web plate of the wide flange cross section; where r is the radius of the k-area. However, in this case, the computed capping stress was increased by 20 % because the regression equation neglects the interaction of flange and web plate buckling. A regularization parameter $\alpha_{reg} = 0.32$ is obtained for the HSS profile that is idealized with four web plates. The corresponding regularization parameters of the web and flange plates of the wide flange cross section are equal to $\alpha_{reg,web} = 0.44$ and $\alpha_{reg,flange} = 0.18$, respectively.

In parallel with the fiber-based simulations in OpenSees, an additional set of simulations is carried out in Abaqus for comparison purposes. These simulations are conducted by following the modeling guidelines according to Suzuki (2018) and Hartloper (2021), for HSS and wide flange beam-columns, respectively. In both cases, shell elements are employed along with the UVC constitutive relation to take into account plasticity. The input material parameters reported in Hartloper et al. (2021) are assumed for the A500 grade B and the A992 grade 50 structural steels.

Figs. 9(a) and 10(a) compare the moment - rotation relations for the cantilever steel beam-column elements. Superimposed in the same figure are the experimental data as well as the corresponding predictions from the Abaqus simulations. From these figures, it is evident that the developed constitutive formulation can predict relatively well both the postyield and the postbuckling response of both steel beam-columns under monotonic loading, regardless of their employed cross section. A similar level of agreement is noted for the axial shortening–rotation relations [Figs. 9(b) and 10(b)].

Figs. 9(c)–10(d) depict the stress distribution across the cross sectional depth of the HSS and the wide flange profiles, respectively. Both figures suggest that after reaching the capping point in the moment-chord rotation relation (point B), the neutral axis (defined as the point where the axial stress σ_{11} is equal to zero)

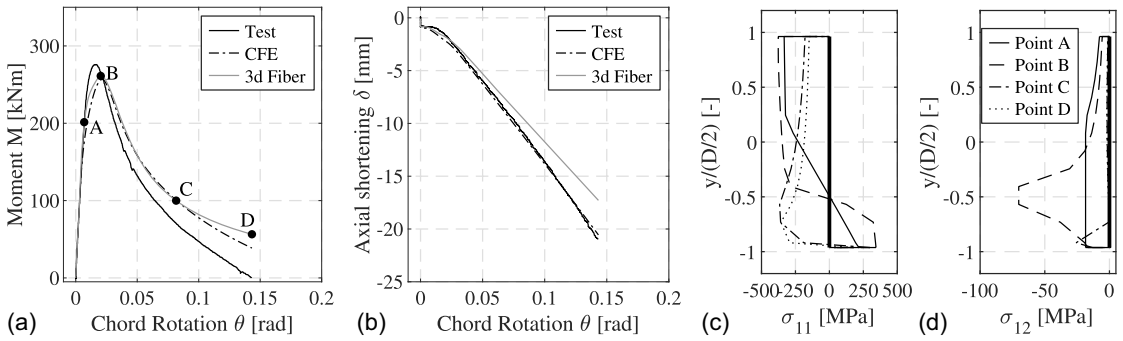

Fig. 9. Model validation with steel HSS column test: (a) moment-chord rotation relation; (b) axial shortening-chord rotation relation; (c) axial stress distribution; and (d) shear stress distribution. (Experimental data from Suzuki and Lignos 2021, © ASCE.)

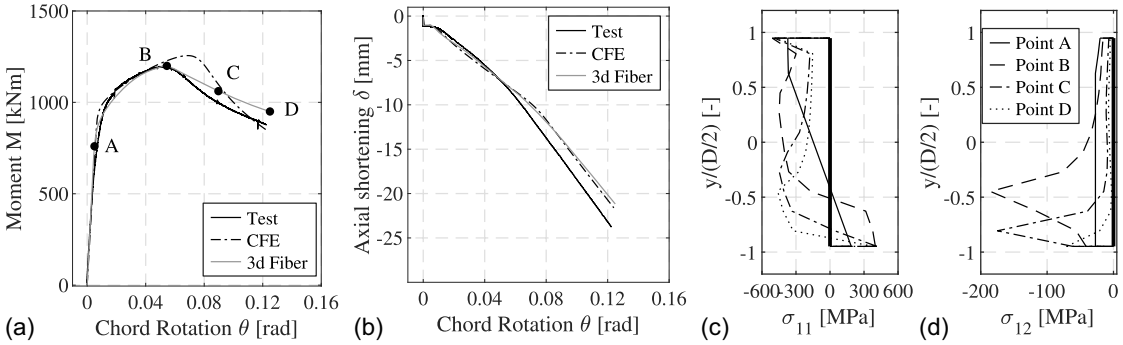

Fig. 10. Model validation with steel wide flange column test: (a) moment-chord rotation relation; (b) axial shortening-chord rotation relation; (c) axial stress distribution; and (d) shear stress distribution. (Experimental data from Cravero et al 2020, © ASCE.)

descends toward the tension-loaded fibers. This shift in the neutral axis location is attributed to the fact that the fibers loaded in tension exhibit elastic unloading to maintain the equilibrium within the cross section after the onset of softening in the fibers loaded in compression. While the featured experimental data refer to the response of cantilever beam-columns under planar monotonic loading, the corresponding simulations trace a complex multiaxial stress state that arises due to the interaction of flexure-axial-shear deformations in the presence of softening due to inelastic local buckling. For instance, referring to Figs. 9(d) and 10(d), the shear stress σ_{12} is maximum at the neutral axis location. Upon further loading, in the descending branch of the moment-rotation relation, the location of the maximum shear stress shifts and follows the neutral axis location in the axial stress distribution. Interestingly, once softening commences at a compressive fiber, the shear stress at that fiber also decreases. This is attributed to the fact that, during softening, the multiaxial ellipsoid yield surface shrinks, thereby reducing both the axial and shear stresses within that fiber. The reduction in the axial and shear stresses within a fiber results into a loss of the axial, shear and flexural load carrying capacity at the cross-sectional level and subsequently at the member level. The preceding indicate the importance of capturing the interaction of axial load, bending and shear in the postbuckling regime.

It is crucial to recognize that the stress distributions given by the proposed modeling approach are contingent upon the fiber-based beam-column element formulation. For instance, as depicted in Figs. 9(d) and 10(d), notable shear stresses σ_{12} are observed in the flanges of HSS and wide-flange sections, which may not be realistic. Heredia Rosa (2024) provides a more comprehensive comparison of the axial and shear stress distributions for both HSS and wide-flange sections. This comparison contrasts the distributions obtained from detailed Abaqus (ABAQUS 2019) shell continuum finite element simulations with those obtained from the utilized 3D Timoshenko force-based beam-column element. The estimated stress distributions can nonetheless be useful for obtaining a qualitative understanding of force redistributions within a member experiencing nonlinear geometric instabilities but one should always be mindful of the important role that the element formulation plays.

It may be argued that these simulations are not sufficient to illustrate the material model performance and that applications to statically indeterminate members would be more appropriate. In this regard, additional simulations were conducted but for the sake of brevity are not shown herein. These simulations indicate that the proposed modeling approach can estimate relatively well the moment-chord rotation relation and axial shortening-chord rotation relation of fixed-fixed wide flange steel beam-columns under monotonic loading. These results can be consulted in Heredia Rosa (2024).

Limitations and Future Work

The proposed softening section constitutive formulation has been developed for simulating the monotonic behavior of steel beam-columns while exhibiting flexural yielding and inelastic local buckling. Member effects (e.g., lateral torsional buckling) are not addressed herein as it is outside the scope of the present paper and it

is conditioned on available element formulations that can indeed capture interactive buckling. The authors are working toward this objective, including advancements at the element level (Maity et al. 2023). Other element formulations (Le Corvec 2012) are also suitable to address the same issue.

Although the proposed formulation is quite flexible, cases where the steel cross section is composed of plates with boundary conditions other than those discussed herein have not been explicitly studied. Moreover, the exploited yield line mechanisms, which are used to capture generic insights of response, exhibit certain limitations with regards to simplified boundary conditions, the geometric symmetry as well as the loading. In the proposed formulations, web and flange plates with idealized boundary conditions have been considered by neglecting the interactions between the two. While this is a simplification, it should be further considered in subsequent parametric studies with members featuring various cross-sectional geometries. This is outside the scope of the present paper. Moreover, the proposed material formulation with softening does not currently address inelastic cyclic buckling, which is typical when earthquake effects on structures are to be addressed.

The material law formulation proposed herein to model inelastic buckling of steel plates is suitable to represent member-level response of steel HSS and wide-flange beam columns subjected to flexure-dominant loading conditions. This is demonstrated by the moment-chord rotation and axial shortening-chord rotation fiber-model comparisons with experimental data. However, the proposed material law formulation should be further evaluated and refined when shear dominant of shear-flexure interaction is of interest. Moreover, the material model has been thoroughly examined under quasi-static loading conditions at a given temperature. Rate effects have not been considered.

The predicted strain and stress fields at the section and fiber-level shall be treated with caution particularly in the postpeak response regime as the fiber-based modeling approach assumes that plane sections remain plane and inelastic local buckling is modeled implicitly through a softening material model. Moreover, because the section and fiber-level results are contingent on the employed element formulation, further investigation is necessary to assess the impact of the proposed multiaxial material law formulation with softening within a 3-dimensional fiber-based beam-column element more capable of accurately capturing stress distributions (e.g., shear within the cross section).

Although a regularization procedure has been proposed to tackle the strain localization and mesh dependency in the presence of the softening material response, this could be further enriched with a nonlocal section deformation approach within a 3-dimensional fiber-based beam-column element. However, this, again is an issue addressed at the element-level and not at the material scale. The advantage of tackling the strain localization through a nonlocal formulation is that this approach does not require the calibration of a case specific reference dissipated energy such as that discussed in the present paper. Examples of nonlocal formulations for 2-dimensional fiber-based simulations are available in the literature (Sideris and Salehi 2016; Kolwankar et al. 2020).

Summary and Conclusions

This paper proposes a novel multiaxial plasticity formulation for simulating inelastic local buckling in fiber-based beam-column elements under monotonic loading. The proposed material model is established on the basis of rate-independent metal plasticity. In the pre-peak response and under a compressive stress state, the proposed model follows J2 plasticity in an identical manner with the corresponding tensile loading. An ellipsoidal yield surface has been developed that exhibits shrinkage when a softening response is anticipated under compressive stresses. This is achieved by formulating an appropriate evolution rule for the parameter governing the compressive yield surface evolution. As such, the proposed constitutive formulation is general and can depict a wide range of softening phenomena. The primary equations of the proposed return mapping algorithms are established, along with the consistent tangent moduli for the main loading stages.

The proposed constitutive relation with softening is then formulated for typical steel plates exhibiting inelastic local buckling under monotonic loading. Their boundary conditions idealize those in plates composing hollow square sections (HSS) and wide flange cross sections. While this idealization is convenient, it neglects the coupling between the flange and webs. Appropriate yield line mechanisms are proposed and validated with continuum finite element simulations on steel plates featuring two characteristic boundary conditions. The yield line mechanisms facilitate the development of an evolution rule for the compressive yield surface with softening. The multiaxial constitutive formulation simulates inelastic steel plate buckling relatively well based on direct comparisons with simulated data from continuum finite element simulations.

In order to mitigate the mesh-dependency due to strain localization in the presence of softening in typical fiber-based beam-column elements (i.e., displacement- or force-based), a regularization procedure is developed for the proposed constitutive formulation. The proposed regularization procedure is based on equating the dissipated energy calibrated from a continuum finite element simulation or an experiment with the selected plate, to the dissipated energy over the integration section where strain localization is expected in the beam-column element.

The formulated constitutive relation is implemented into an open-source simulation platform, and is then assigned to the cross section of a 3-dimensional force-based beam-column element. The overall modeling approach is validated with experiments and continuum finite element simulations on steel HSS and wide flange cantilever beam-columns subjected to planar monotonic loading. Comparisons of the simulated and measured moment-chord rotation and axial shortening-chord rotation of physically tested steel beam-columns demonstrate a noteworthy accuracy both in the pre- and postpeak response regime. Limitations of the proposed multiaxial constitutive formulation are presented along with suggestions for future work.

Data Availability Statement

Some or all data, models, or code generated or used during the study are available in a repository online in accordance with funder data retention policies.

Acknowledgments

This study is based on work supported by the Swiss National Science Foundation (Award No. 200021_188476), an internal research grant from École Polytechnique Fédérale de Lausanne, and by the US National Science Foundation (Grant #CMMI-1926202). The financial support is gratefully acknowledged. Any opinions, findings, and conclusions or recommendations expressed in this paper are those of the authors and do not necessarily reflect the views of the sponsors.

Notation

The following symbols are used in this paper:

a = isotropic hardening rate parameter for yield surface reduction;
b = isotropic hardening rate parameter for cyclic hardening;
b_{1c} = constant term controlling the evolution of χ_{1c};
b/t = plate slenderness;
c_{1c} = constant term enabling buckling prior to yielding;
$\boldsymbol{C}$ = matrix of elastic tangent moduli;
$\boldsymbol{C}^{ep}$ = matrix of consistent tangent moduli;
C_k = kinematic hardening magnitude for kth backstress;
D_∞ = isotropic hardening magnitude for yield surface reduction;
G = reference dissipated energy;
I_1 = first invariant of the stress tensor;
J_2 = second invariant of the deviatoric stress tensor;
L = member length;
L_b = unbraced member length;
L_{IP} = integration point length;
L_b/r_y = member slenderness ratio;
M = member base moment;
m_p = plastic moment per unit length in the yield lines;
m_η = bending moment per unit length in the inclined yield lines;
$m_\perp$ = bending moment per unit length in the perpendicular yield line;
$\boldsymbol{n}$ = unit vector normal to yield surface;
$\boldsymbol{p}$ = projection vector;
$\boldsymbol{P}$ = projection matrix;
P = member axial load demand;
P_y = member axial resistance;
Q_∞ = isotropic hardening magnitude for cyclic hardening;
$T = (\sigma_m/\sigma_{VM})$ = stress triaxiality;
$\boldsymbol{\alpha}$ = backstress vector;
α_{1c} = free parameter related to the stress triaxiality in the plates yield lines;
α_{reg} = regularization parameter;
β_i = regression parameter i;
γ_k = kinematic hardening rate parameter for kth backstress;
δ = axial shortening;
ε_{eff} = effective strain;
$\boldsymbol{\varepsilon}$ = total strain vector;
$\boldsymbol{\varepsilon}^e$ = elastic strain vector;
$\boldsymbol{\varepsilon}^p$ = plastic strain vector;
$\boldsymbol{\varepsilon}^{pb}$ = postbuckling strain vector;
ε_{11}^{pb} = axial postbuckling strain component;
ε_{eq}^{p} = equivalent plastic strain;
ε_{eq}^{pb} = equivalent postbuckling strain;
η = angle between the plate edge and the inclined yield line;
θ = member chord rotation;
λ_{pb} = postbuckling multiplier;
Λ = plate half-length;
$\boldsymbol{\xi}$ = relative stress;
σ_{eff} = effective stress;
$\boldsymbol{\sigma}$ = stress vector;
σ_{dm} = stress at buckling length stabilization;
σ_{c0} = initial capping stress;
$\sigma_m = (1/3)(\sigma_{11} + \sigma_{22} + \sigma_{33})$ = mean stress;
σ_{VM} = von-Mises stress;
σ_y = yield stress;
$\sigma_{y,0}$ = initial yield stress;
σ/σ_y = ratio from the plates yield line mechanisms controlling the evolution of χ_{1c};
ϕ^{ELL} = compressive ellipsoid yield surface;
ϕ^{VM} = von-Mises yield surface; and
χ_{1c} = parameter controlling the compressive yield surface radius parallel to the hydrostatic axis.

References

ABAQUS. 2019. *ABAQUS analysis user's manual version 6.19*. Providence, RI: Dassault Systems Simulia Corporation.

Abramowitz, M., and I. A. Stegun. 1965. "Handbook of mathematical functions: With formulas, graphs, and mathematical tables." In *Dover books on mathematics*, 9th ed. New York: Dover Publications.

AISC. 2022. *Seismic provisions for structural steel buildings*. ANSI/AISC 341-22. Chicago: AISC.

ASCE. 2023. *Seismic evaluation and retrofit of existing buildings*. ASCE/SEI 41-23. Reston, VA: ASCE.

Bai, Y., and X. Lin. 2015. "Numerical simulation on seismic collapse of thin-walled steel moment frames considering post local buckling behavior." *Thin-Walled Struct.* 94 (Sep): 424–434. https://doi.org/10.1016/j.tws.2015.04.033.

Bai, Y., Y. Shi, and K. Deng. 2016. "Collapse analysis of high-rise steel moment frames incorporating deterioration effects of column axial force–bending moment interaction." *Eng. Struct.* 127 (Mar): 402–415. https://doi.org/10.1016/j.engstruct.2016.09.005.

Bierlaire, M. 2015. *Optimization: Principles and algorithms*. 2nd ed. Lausanne, Switzerland: EPFL.

CEN (European Committee for Standardization). 2005a. *Eurocode 3: Design of steel structures—Part 1-1: General rules and rules for buildings*. EN1993-1-1. Brussels, Belgium: CEN.

CEN (European Committee for Standardization). 2005b. *Eurocode 8: Design of structures for earthquake resistance—Part 3: Assessment and retrofitting of buildings*. EN1998-3. Brussels, Belgium: CEN.

Chaboche, J.-L., K. Dang Van, and G. Cordier. 1979. "Modelization of the strain memory effect on the cyclic hardening of 316 stainless steel." In *Proc., 5th Int. Conf. on Structural Mechanics in Reactor Technology*. Berlin: North-Holland.

Chen, W.-F., and D.-J. Han. 1988. *Structural plasticity*. New York: Springer.

Coleman, J., and E. Spacone. 2001. "Localization issues in force-based frame elements." *J. Struct. Eng.* 127 (11): 1257–1265. https://doi.org/10.1061/(ASCE)0733-9445(2001)127:11(1257).

Cravero, J., A. Elkady, and D. G. Lignos. 2020. "Experimental evaluation and numerical modeling of wide-flange steel columns subjected to constant and variable axial load coupled with lateral drift demands." *J. Struct. Eng.* 146 (3): 04019222. https://doi.org/10.1061/(ASCE)ST.1943-541X.0002499.

Crisfield, M. A. 1991. Vol. 22 of *Non-linear finite element analysis of solids and structures*. New York: Wiley.

de Castro e Sousa, A., Y. Suzuki, and D. Lignos. 2020. "Consistency in solving the inverse problem of the Voce-Chaboche constitutive model for plastic straining." *J. Eng. Mech.* 146 (9): 04020097. https://doi.org/10.1061/(ASCE)EM.1943-7889.0001839.

Dhakal, R. P., and K. Maekawa. 2002a. "Modeling for postyield buckling of reinforcement." *J. Struct. Eng.* 128 (9): 1139–1147. https://doi.org/10.1061/(ASCE)0733-9445(2002)128:9(1139).

Dhakal, R. P., and K. Maekawa. 2002b. "Path-dependent cyclic stress–strain relationship of reinforcing bar including buckling." *Eng. Struct.* 24 (11): 1383–1396. https://doi.org/10.1016/S0141-0296(02)00080-9.

Di Re, P. 2017. "3D beam-column finite elements under tri-axial stress-strain states: Non-uniform shear stress distribution and warping." Ph.D. thesis, Dept. of Structural and Geotechnical Engineering, Sapienza Universita di Roma.

Di Re, P., and D. Addessi. 2018. "A mixed 3D corotational beam with cross-section warping for the analysis of damaging structures under large displacements." *Meccanica* 53 (6): 1313–1332. https://doi.org/10.1007/s11012-017-0749-3.

Drucker, D. C., and W. Prager. 1952. "Soil mechanics and plastic analysis or limit design." *Q. Appl. Math.* 10 (2): 157–165. https://doi.org/10.1090/qam/48291.

Elkady, A., and D. G. Lignos. 2018a. "Full-scale testing of deep wide-flange steel columns under multiaxis cyclic loading: Loading sequence, boundary effects, and lateral stability bracing force demands." *J. Struct. Eng.* 144 (2): 04017189. https://doi.org/10.1061/(ASCE)ST.1943-541X.0001937.

Elkady, A., and D. G. Lignos. 2018b. "Improved seismic design and nonlinear modeling recommendations for wide-flange steel columns." *J. Struct. Eng.* 144 (9): 04018162. https://doi.org/10.1061/(ASCE)ST.1943-541X.0002166.

Fogarty, J., and S. El-Tawil. 2016. "Collapse resistance of steel columns under combined axial and lateral loading." *J. Struct. Eng.* 142 (1): 04015091. https://doi.org/10.1061/(ASCE)ST.1943-541X.0001350.

Frederick, C., and P. Armstrong. 2007. "A mathematical representation of the multiaxial Bauscinger effect." *Mater. High Temp.* 24 (1): 1–26. https://doi.org/10.3184/096034007X207589.

Gomes, A., and J. Appleton. 1997. "Nonlinear cyclic stress-strain relationship of reinforcing bars including buckling." *Eng. Struct.* 19 (10): 822–826. https://doi.org/10.1016/S0141-0296(97)00166-1.

Gruttmann, F., R. Sauer, and W. Wagner. 2000. "Theory and numerics of three-dimensional beams with elastoplastic material behaviour." *Int. J. Numer. Methods Eng.* 48 (12): 1675–1702. https://doi.org/10.1002/1097-0207(20000830)48:12<1675::AID-NME957>3.0.CO;2-6.

Hartloper, A. R. 2021. "Reduced-order models for simulating coupled geometric instabilities in steel beam-columns under inelastic cyclic straining." Ph.D. thesis, Dept. of Architecture, Civil and Environmental Engineering, Ecole Polytechnique Federale Lausanne.

Hartloper, A. R., A. de Castro e Sousa, and D. G. Lignos. 2021. "Constitutive modeling of structural steels: Nonlinear isotropic/kinematic hardening material model and its calibration." *J. Struct. Eng.* 147 (4): 04021031. https://doi.org/10.1061/(ASCE)ST.1943-541X.0002964.

Hartloper, A. R., A. de Castro e Sousa, and D. G. Lignos. 2022a. "Best-fit constraint equations for coupling mixed-dimension simulation models with wide flange cross sections." *Finite Elem. Anal. Des.* 208 (Apr): 103782. https://doi.org/10.1016/j.finel.2022.103782.

Hartloper, A. R., A. de Castro e Sousa, and D. G. Lignos. 2022b. "Warping-inclusive kinematic coupling in mixed-dimension macro models for steel wide flange beam columns." *J. Struct. Eng.* 148 (2): 04021253. https://doi.org/10.1061/(ASCE)ST.1943-541X.0003211.

Hartloper, A. R., S. Ozden, A. de Castro e Sousa, and D. G. Lignos. 2023. "Uniaxial cyclic and tensile tests on structural metallic materials." *J. Struct. Eng.* 149 (5): 04723001. https://doi.org/10.1061/JSENDH.STENG-12037.

Heredia Rosa, D. I. 2024. "A softening constitutive law and gradient-inelastic fiber-based element for 3-dimensional frame simulations under seismic excitations." Ph.D. thesis, Dept. of Architecture, Civil and Environmental Engineering, Ecole Polytechnique Federale Lausanne.

Heredia Rosa, D.-I., A. de Castro e Sousa, and D. G. Lignos. 2023. "Monotonic material model repository." Accessed June 9, 2023. https://github.com/RESSLab-Team/MonotonicPlateBucklingModel.

Hopperstad, O. S., and S. Remseth. 1995. "A return mapping algorithm for a class of cyclic plasticity models." *Int. J. Numer. Methods Eng.* 38 (4): 549–564. https://doi.org/10.1002/nme.1620380404.

Huber, M. T. 2004. "Specific work of strain as a measure of material effort." *Arch. Mech.* 56 (3): 173–190.

Ibarra, L. F., R. A. Medina, and H. Krawinkler. 2005. "Hysteretic models that incorporate strength and stiffness deterioration." *Earthquake Eng. Struct. Dyn.* 34 (12): 1489–1511. https://doi.org/10.1002/eqe.495.

Kashani, M. M., L. N. Lowes, A. J. Crewe, and N. A. Alexander. 2015. "Phenomenological hysteretic model for corroded reinforcing bars including inelastic buckling and low-cycle fatigue degradation." *Comput. Struct.* 156 (Apr): 58–71. https://doi.org/10.1016/j.compstruc.2015.04.005.

Kemp, A. R. 1985. "Interaction of plastic local and lateral buckling." *J. Struct. Eng.* 111 (10): 2181–2196. https://doi.org/10.1061/(ASCE)0733-9445(1985)111:10(2181).

Kolupaev, V. A. 2018. "Equivalent stress concept for limit state analysis." Vol. 86 of *Advanced structured materials*. Cham, Switzerland: Springer.

Kolwankar, S., A. Kanvinde, M. Kenawy, D. Lignos, and S. Kunnath. 2018. "Simulating local buckling-induced softening in steel members using an equivalent nonlocal material model in displacement-based fiber elements." *J. Struct. Eng.* 144 (10): 04018192. https://doi.org/10.1061/(ASCE)ST.1943-541X.0002189.

Kolwankar, S., A. Kanvinde, M. Kenawy, D. Lignos, and S. Kunnath. 2020. "Simulating cyclic local buckling–induced softening in steel beam-columns using a nonlocal material model in displacement-based fiber elements." *J. Struct. Eng.* 146 (1): 04019174. https://doi.org/10.1061/(ASCE)ST.1943-541X.0002457.

Krawinkler, H., M. Zohrei, B. Lashkari-Irvani, N. Cofie, and H. Hadidi-Tamjed. 1983. *Recommendations for experimental studies on the seismic behavior of steel components and materials*. Rep. No. 61. Stanford, CA: Stanford Univ.

Krishnan, S. 2010. "Modified elastofiber element for steel slender column and brace modeling." *J. Struct. Eng.* 136 (11): 1350–1366. https://doi.org/10.1061/(ASCE)ST.1943-541X.0000238.

Le Corvec, V. 2012. "Nonlinear 3d frame element with multi-axial coupling under consideration of local effects." Ph.D. thesis, Dept. of Civil and Environmental Engineering, Univ. of California Berkeley.

Lee, J., and G. L. Fenves. 1998. "Plastic-damage model for cyclic loading of concrete structures." *J. Eng. Mech.* 124 (8): 892–900. https://doi.org/10.1061/(ASCE)0733-9399(1998)124:8(892).

Lignos, D. G., and H. Krawinkler. 2011. "Deterioration modeling of steel components in support of collapse prediction of steel moment frames under earthquake loading." *J. Struct. Eng.* 137 (11): 1291–1302. https://doi.org/10.1061/(ASCE)ST.1943-541X.0000376.

Lubliner, J. 2008. *Plasticity theory.* New York: Dover.

Lubliner, J., J. Oliver, S. Oller, and E. Oñate. 1989. "A plastic-damage model for concrete." *Int. J. Solids Struct.* 25 (3): 299–326. https://doi.org/10.1016/0020-7683(89)90050-4.

MacRae, G. A. 1989. "The seismic response of steel frames." Ph.D. thesis, Dept. of Civil Engineering, Univ. of Canterbury.

Maity, A., A. Kanvinde, D. I. Heredia Rosa, A. de Castro e Sousa, and D. G. Lignos. 2023. "A displacement-based fiber element to simulate interactive lateral torsional and local buckling in steel members." *J. Struct. Eng.* 149 (5): 04023045. https://doi.org/10.1061/JSENDH.STENG-11889.

Mander, J. B., M. J. N. Priestley, and R. Park. 1988. "Theoretical stress-strain model for confined concrete." *J. Struct. Eng.* 114 (8): 1804–1826. https://doi.org/10.1061/(ASCE)0733-9445(1988)114:8(1804).

Martins, J. R. R. A., P. Sturdza, and J. J. Alonso. 2003. "The complex-step derivative approximation." *ACM Trans. Math. Software* 29 (3): 245–262. https://doi.org/10.1145/838250.838251.

Mazars, J., P. Kotronis, F. Ragueneau, and G. Casaux. 2006. "Using multifiber beams to account for shear and torsion: Applications to concrete structural elements." *Comput. Methods Appl. Mech. Eng.* 195 (52): 7264–7281. https://doi.org/10.1016/j.cma.2005.05.053.

McKenna, F. 1997. "Object-oriented finite element programming: Frameworks for analysis, algorithms and parallel computing." Ph.D. thesis, Dept. of Civil Engineering, Univ. of California Berkeley.

Möller, M., B. Johansson, and P. Collin. 1997. "A new analytical model of inelastic local flange buckling." *J. Constr. Steel Res.* 43 (1–3): 43–63. https://doi.org/10.1016/S0143-974X(97)00025-4.

Navarro Gregori, J., P. Miguel Sosa, M. Fernández Prada, and F. C. Filippou. 2007. "A 3D numerical model for reinforced and prestressed concrete elements subjected to combined axial, bending, shear and torsion loading." *Eng. Struct.* 29 (12): 3404–3419. https://doi.org/10.1016/j.engstruct.2007.09.001.

Newell, J. D., and C.-M. Uang. 2008. "Cyclic behavior of steel wide-flange columns subjected to large drift." *J. Struct. Eng.* 134 (8): 1334–1342. https://doi.org/10.1061/(ASCE)0733-9445(2008)134:8(1334).

Ozkula, G., J. Harris, and C.-M. Uang. 2017a. "Classifying cyclic buckling modes of steel wide-flange columns under cyclic loading." In *Proc., Structures Congress 2017*, 155–167. Reston, VA: ASCE.

Ozkula, G., J. Harris, and C.-M. Uang. 2017b. "Observations from cyclic tests on deep, slender wide-flange structural." *Eng. J.* 54 (1): 45. https://doi.org/10.62913/engj.v54i1.1109.

Ribeiro, F. L. A., A. R. Barbosa, M. H. Scott, and L. C. Neves. 2015. "Deterioration modeling of steel moment resisting frames using finite-length plastic hinge force-based beam-column elements." *J. Struct. Eng.* 141 (2): 04014112. https://doi.org/10.1061/(ASCE)ST.1943-541X.0001052.

Saritas, A., and F. C. Filippou. 2009. "Frame element for metallic shear-yielding members under cyclic loading." *J. Struct. Eng.* 135 (9): 1115–1123. https://doi.org/10.1061/(ASCE)ST.1943-541X.0000041.

Sediek, O. A., T.-Y. Wu, J. McCormick, and S. El-Tawil. 2020. "Collapse behavior of hollow structural section columns under combined axial and lateral loading." *J. Struct. Eng.* 146 (6): 04020094. https://doi.org/10.1061/(ASCE)ST.1943-541X.0002637.

Sideris, P., and M. Salehi. 2016. "A gradient inelastic flexibility-based frame element formulation." *J. Eng. Mech.* 142 (7): 04016039. https://doi.org/10.1061/(ASCE)EM.1943-7889.0001083.

Simo, J., and T. Hughes. 1998. "Computational inelasticity." In *Interdisciplinary applied mathematics*. New York: Springer.

Spacone, E., V. Ciampi, and F. Filippou. 1996. "Mixed formulation of nonlinear beam finite element." *Comput. Struct.* 58 (1): 71–83. https://doi.org/10.1016/0045-7949(95)00103-N.

Suzuki, Y. 2018. "Earthquake-induced collapse of steel moment resisting frames with conventional and high performance steel columns." Ph.D. thesis, Dept. of Civil Engineering and Applied Mechanics, McGill Univ.

Suzuki, Y., and D. G. Lignos. 2020. "Fiber-based hysteretic model for simulating strength and stiffness deterioration of steel hollow structural section columns under cyclic loading." *Earthquake Eng. Struct. Dyn.* 49 (15): 1702–1720. https://doi.org/10.1002/eqe.3324.

Suzuki, Y., and D. G. Lignos. 2021. "Experimental evaluation of steel columns under seismic hazard-consistent collapse loading protocols." *J. Struct. Eng.* 147 (4): 04021020. https://doi.org/10.1061/(ASCE)ST.1943-541X.0002963.

Taucer, F. F., E. Spacone, and F. C. Filippou. 1991. *A fiber beam-column element for seismic response analysis of reinforced concrete structures*. Rep. No. UCB/EERC-91/17. Berkeley, CA: Univ. of California Berkeley.

Tort, C., and J. F. Hajjar. 2010. "Mixed finite-element modeling of rectangular concrete-filled steel tube members and frames under static and dynamic loads." *J. Struct. Eng.* 136 (6): 654–664. https://doi.org/10.1061/(ASCE)ST.1943-541X.0000158.

Varma, A. H., R. Sause, J. M. Ricles, and Q. Li. 2005. "Development and validation of fiber model for high-strength square concrete-filled steel tube beam-columns." *ACI Struct. J.* 102 (1): 73–84.

Wang, M., Y. Shi, and Y. Wang. 2012. "Equivalent constitutive model of steel with cumulative degradation and damage." *J. Constr. Steel Res.* 79 (Jan): 101–114. https://doi.org/10.1016/j.jcsr.2012.07.028.

Wasserman, L. 2004. "All of statistics: A concise course in statistical inference." In *Springer texts in statistics*. New York: Springer.

Wu, T.-Y., S. El-Tawil, and J. McCormick. 2018. "Seismic collapse response of steel moment frames with deep columns." *J. Struct. Eng.* 144 (9): 04018145. https://doi.org/10.1061/(ASCE)ST.1943-541X.0002150.